Validation of pressure-impulse theory for standing wave impact loading on vertical hydraulic structures with short overhangs

de Almeida , Ermano; Hofland, Bas

DOI
10.1016/j.coastaleng.2020.103702

Publication date
2020

Document Version
Final published version

Published in
Coastal Engineering

Citation (APA)
de Almeida , E., & Hofland, B. (2020). Validation of pressure-impulse theory for standing wave impact loading on vertical hydraulic structures with short overhangs. *Coastal Engineering*, *159*, Article 103702. https://doi.org/10.1016/j.coastaleng.2020.103702

Coastal Engineering 159 (2020) 103702

Contents lists available at ScienceDirect

Coastal Engineering

journal homepage: http://www.elsevier.com/locate/coastaleng

Validation of pressure-impulse theory for standing wave impact loading on vertical hydraulic structures with short overhangs

Ermano de Almeida *, Bas Hofland

Department of Hydraulic Engineering, Faculty of Civil Engineering and Geosciences, Delft University of Technology, Stevinweg 1, 2628 CN, Delft, the Netherlands

ARTICLE INFO

Keywords:
Wave impacts
Impulsive loading
Hydraulic structures
Overhangs
Pressure-impulse
Physical modelling

ABSTRACT

The applicability of pressure-impulse theory is evaluated for predicting wave impact loading magnitudes for non-breaking standing wave impacts on vertical hydraulic structures with relatively short overhangs. To this end, tests were carried out on a schematized but realistic configuration with low steepness regular wave impacts on a straight overhang perpendicular to a vertical wall. This paper aims to fill the existing knowledge gap on this type of wave impact with reliable and simple expressions. Pressure-impulses and force-impulses are the wave impact loading magnitudes considered in this study, which are defined as the integral of the impulsive pressures/forces over time during a wave impact. These impulses can be used to determine the resulting stresses in a structure for sudden, impulsive loads. The proposed theoretical model is based on the pressure-impulse theory and validated with laboratory experiments. The laboratory tests are done with regular waves for relatively short overhangs, with ratios of wave length to overhang length between 12.1 and 43.6, and ratios of overhang height to overhang length of 3 and 6. Thus, the theory is verified for conditions where the wave impact takes place along the full length of the overhang. From the experimental results, a mean effective bounce-back factor $\beta = 1.17$ is obtained, accounting for the bounce-back effect of entrapped air and other secondary sources of discrepancies between theoretical and experimental results. The standard deviation of β for all the different tests is $\sigma_\beta = 0.11$. This method seems suitable for carrying out preliminary loading estimations, including the pressure-impulse profile at the wall and the total force-impulse at the wall. This study also shows that the force-impulse is a more stable magnitude compared with the force peaks, with about half the relative standard deviation. The impulses predicted by this model are recommended to be coupled with fluid-structure interaction models for analysing the response of the loaded structure.

1. Introduction

In the coming years and decades, various new hydraulic structures will be constructed around the world at coastal areas, delta regions, lakes or reservoirs. In addition, several of the existing hydraulic structures will be renovated after reaching the end of the envisaged design lifetime or due to increasing safety standards and/or loading conditions. Wave loads often play a key role in the design of these structures. This leads to a demand for extended knowledge on the design of hydraulic structures subjected to wave impacts. Three wave impact configurations can be distinguished in Fig. 1. Among these three types of wave impacts, this study addresses wave impacts on overhang configurations, caused by non-breaking reflecting waves.

Previous research has mainly focused on the study of wave impacts caused by breaking waves on vertical structures (Bagnold, 1939; Minikin, 1950; Goda, 1974; Takahashi et al., 1994; Oumeraci et al., 2001; Cuomo et al., 2010). In addition, vertical structures with overhangs have been studied but only subjected to breaking wave impacts (Kisacik et al., 2014). Wave impacts caused by overtopping waves have been also studied in the last years (Chen et al., 2015, 2016). The study from Dias and Ghidaglia (2018) presents recent developments of numerical and experimental models and tools for evaluating slamming magnitudes on ship hulls, natural gas tanks and offshore structures. In contrast, a significant knowledge gap exists on wave impacts caused by standing waves on vertical structures with overhangs, such as crest walls, lock gates, sluice gates, dewatering sluices, flood gates and storm surge barriers (De Almeida et al., 2019; Ramkema, 1978). The study presented hereafter addresses this knowledge gap on wave impacts caused by non-breaking standing waves on a vertical structure with a relatively small overhang and a flat bottom, considering the

* Corresponding author.
E-mail address: e.dealmeid@tudelft.nl (E. de Almeida).

https://doi.org/10.1016/j.coastaleng.2020.103702
Received 10 December 2019; Received in revised form 23 March 2020; Accepted 30 March 2020
Available online 9 April 2020

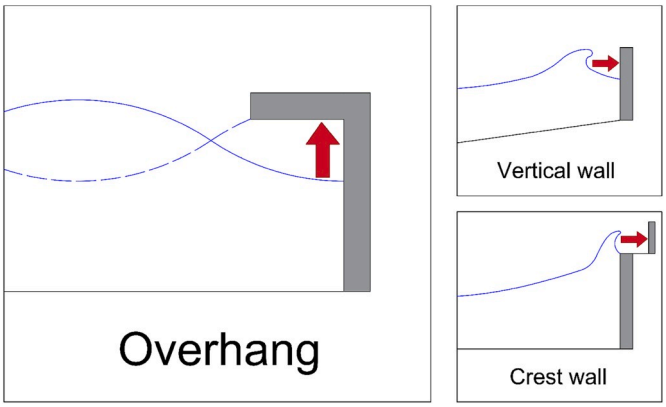

Fig. 1. Main wave impact configurations. Left: Overhang, subjected to non-breaking reflecting wave impacts. Top right: Vertical wall, subjected to breaking waves impacts. Bottom right: Crest wall, subjected to overtopping wave impacts.

pressure-impulse theory and experimental test results.

Fig. 2 shows a cross-section of a flood gate system in the Afsluitdijk in The Netherlands, which is currently undertaking major renovations after more than 80 years of service and additional structures are being built. Such flood gates remain open during low tides in order to allow the water to flow from the lake to the sea. During high tides and storms, these flood gates remain closed in order to avoid the flooding of the hinterland. As it can be observed both from the sea side and from the lake side, overhangs (shown in dark grey) are present in front/back of the gates (shown in red). In such structures, the vertically upwards moving standing wave surface at the vertical wall can produce violent global wave impacts when hitting the rigid horizontal lower overhang surface. Furthermore, wave impacts can take place also locally at the gate reinforcement beams with incident waves from the lake side. Thus, this structure represents an example of conditions where standing waves lead to violent global and local wave impacts, also as it was investigated in the design of the Eastern Scheldt Storm Surge Barrier (Ramkema, 1978). Nevertheless, as mentioned above, many other examples of hydraulic structures with overhangs can be found in coastal areas, delta regions, lakes and reservoirs (Ramkema, 1978; Castellino et al., 2018; Martinelli et al., 2018; Van der Meer et al., 2018). Similar impacts on overhang configurations also occur in nature, for instance on the fracture of cliffs and shore platforms (Herterich et al., 2018).

In Fig. 3 the main hydraulic and structural parameters to be considered in wave impacts on vertical structures with overhangs are shown. This paper focuses on relatively small overhangs, with ratios of wave length (L) to overhang length (W) in the range of $12.1 < L/W < 43.6$, and ratios of overhang height (h) to overhang length (W) of $h/W = 3$ and $h/W = 6$. This study focusses on the conditions with zero freeboard ($d = h$) which leads to the expected maximum wave surface velocity impacting the overhang.

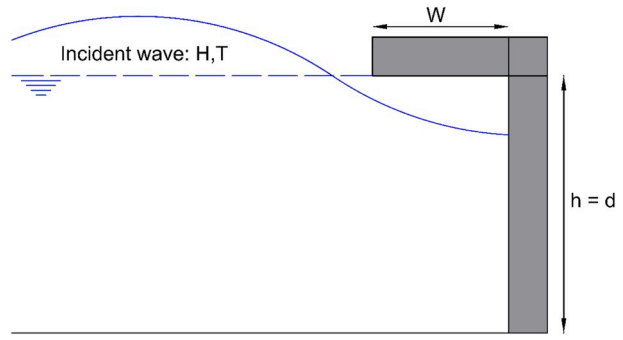

Fig. 3. H: incident wave height; T: incident wave period; d: still water depth; h: overhang height; W: overhang width.

1.1. Literature

Bagnold (1939) presented significant progress to the study of impulsive loading due to wave breaking, including two significant contributions. Firstly, on the study of the effect of air in wave impacts, observing the highest pressure magnitudes when the air cushion is small, but not zero. Secondly, with the observation that although maximum peak pressures present large variations, the area enclosed by the pressure-time curve (which can be defined as pressure-impulse, as shown in Equation (1) was remarkably constant.

$$P(x)_i = \int_{t_0}^{t_1} p(x,t)\cdot dt \tag{1}$$

where $P(x)_i$ [Pa·s] is the pressure-impulse from impact i at location x, $p(x,t)$ [Pa] is the pressure time-series during impact i at location x, t_0 [s] is start of impact i and t_1 [s] is end of impact i.

Extensive experimental tests were carried out in The Netherlands during the design of the Delta Works (1953–1997). For the Eastern Scheldt Storm Surge Barrier design, a large number of tests (Ramkema, 1978; WL, 1977; WL, 1978) studied wave loading on various configurations such as vertical wall and overhangs. Nevertheless, those studies were focused on the design optimization and did not address the definition of general design methods. Furthermore, according to WL, 1979 water can be considered incompressible for wave impact problems in civil engineering structures such as hydraulic structures. On the other hand, according to WL, 1979 the presence of air in wave impacts has a significant effect on aspects such as wave impact magnitudes, duration and variability, and the presence of pressure oscillations in the water body due to the compression and decompression of air pockets.

Also based on experimental results, Kisacik et al. (2014) defined formulas for vertical structures with long overhangs under wave breaking. Moreover, Renzi et al., 2018 studied wave slamming on oscillating water column converters based on wave tank tests. Hofland (2015) carried out experiments in order to study the wave loading on the flood gates of the Afsluitdijk, including the effect of the existing

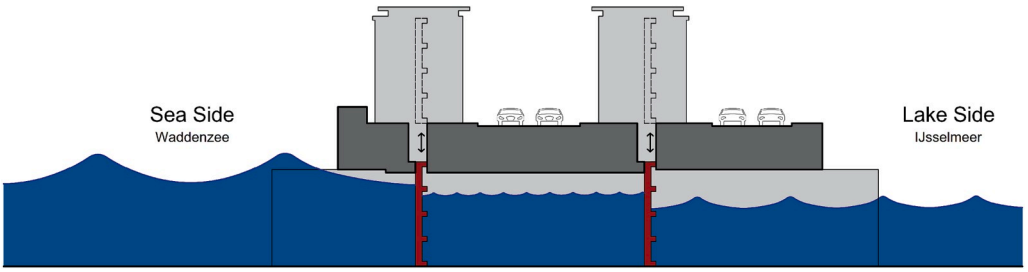

Fig. 2. Impression of an existing flood gate complex in the Afsluitdijk, closed during high water level at the sea side. Standing wave impacts can occur in this flood gate complex at the sea side due to extreme incident waves (global impact on the overhang), and/or at the lake side due to moderate incident waves (global impact on the overhang or local impact on gate reinforcements).

overhang and ventilation gaps. In those tests, a large variation of the measured extreme forces ($\sigma_F/\mu_F = 70\%$) was observed.

Cooker and Peregrine, 1990, 1995 introduced the pressure-impulse theory applied to wave impacts. This theory presents a theoretical model to estimate the wave impact pressure-impulses, based on the Navier-Stokes equation of motion. These two first contributions consider a vertical wall configuration with a horizontally moving body of water, representing a simplified breaking wave, impacting the vertical structure. Later on, Wood and Peregrine (1996) adapted the pressure-impulse theory to conditions where a vertically upward moving body of water impacts a horizontal rigid boundary above the vertical wall. This model is used in this study, as shown in Fig. 4. In addition, Peregrine and Thais, 1996, Wood et al., 2000 and Bredmose et al., 2009 address the effect of air in wave impacts, while Peregrine, 2003 combines all the contributions to the pressure-impulse theory up to that time. Most of the works on the pressure-impulse theory are analytical, with some validation in Wood et al., 2000and Bredmose et al., 2009. The theory is only partially confirmed by measurements in these studies which mainly treat breaking wave impacts. However, this low correspondence is considered to be caused by the very complicated kinematics within a breaking wave (Wood et al., 2000; Peregrine, 2003) that are not fully captured by the assumed constant impact velocity. In this present work, we address a configuration with a potentially much more uniform impact velocity.

For the design of hydraulic structures, Chen et al. (2019) introduce the use of pressure-impulses and force-impulses for the design of hydraulic structures, instead of the peak forces, and proposes a model for obtaining the wave impacts reaction forces. According to this method, the total reaction force of a wave impact is obtained from Equation (2).

$$F_{tot,r} = F_{qs+} + I_{im} \cdot \omega_n \cdot DLF_I \tag{2}$$

where $F_{tot,r}$ [N] is the total reaction force, F_{qs+} [N] is the quasi-static force, I_{im} [N·s] is the total impulsive force-impulse acting on the structure, ω_n [s^{-1}] is the angular natural frequency of the structure and DLF_I [-] is the dynamic load factor of the structure.

For impact durations smaller than one fourth of the longest natural period of the structure ($t_d < T_n/4$), the impact can be regarded as fully impulsive in a structural sense and the dynamic load factor from Equation (2) can be approximated to $DLF_I = 1$. This highlights the importance of considering the structural characteristics in the design of coastal and hydraulic structures under impulsive loads such as wave impacts. These structural characteristics define the response of the structure to impulsive loads, and in consequence the applicability of the impulse for the design or the need of considering the impulse in combination with the impact duration. Furthermore, Tieleman et al. (2019) developed a semi-analytical fluid-structure interaction model that can be used for wave impact loading, which result is the structural response of elastic structures due to such wave impacts.

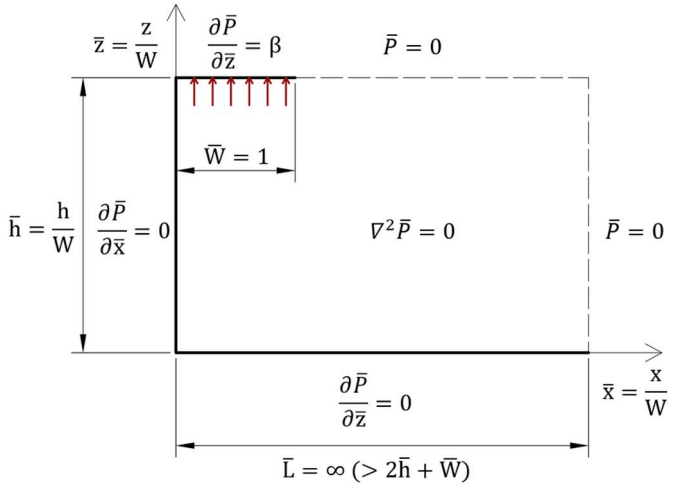

Fig. 4. Dimensionless pressure-impulse model for a vertical impact on a horizontal overhang (based on (Wood and Peregrine, 1996)).

1.2. Paper aims

From the previous sources, a conclusion can be drawn on the various possible advantages of using pressure-impulses and force-impulses for the design of vertical hydraulic structures with overhangs subjected to wave impacts. Those are mainly the observed lower variability (Bagnold, 1939), the availability of a theoretical model that is based on basic principles (Wood and Peregrine, 1996) and the proposed use in the design process (Chen et al., 2019).

Thus, the aim of this study is to validate the use of pressure-impulse theory for predicting wave load magnitudes (i.e. pressure-impulses and force-impulses) on vertical hydraulic structures with overhangs. The applied approach is the validation of the pressure-impulse theory based on laboratory experimental data on a setup that is realistic and strictly resemble the theoretical schematization. The scope of this study includes relatively short overhangs, regular non-breaking standing wave with limited wave steepness ($0.023 < s < 0.042$) and zero freeboard.

Section 2 describes the theoretical model based on the pressure-impulse theory. Section 3 presents the experimental tests carried out. The validation of the theoretical model is carried out in Section 4. Section 5 discusses its applicability and causes of error, while Section 6 summarizes the main conclusions of this study.

2. Theoretical model

This section describes the theoretical model for estimating standing wave impact loadings on vertical structures with overhangs, based on the pressure-impulse theory.

2.1. Pressure-impulse theory

The pressure-impulse concept in Equation (1) (integral of the impulsive pressures over time, during a wave impact) is considered in this theory. Bagnold and other authors (Bagnold, 1939; Richert, 1968), have observed that the pressure-impulse during wave impacts are significantly more constant than other magnitudes, such as pressure peaks.

The pressure-impulse theory is based on the Navier-Stokes equation of motion, for a large-scale motion such that the viscosity and surface tension terms are considered negligible. Considering that the wave impact occurs in such a small period of time, gravity and the non-linear convective terms can also be neglected. Gravity is neglected given that during those violent impacts accelerations are assumed to be much larger than gravity. The non-linear convective terms are neglected given that those violent impacts have a short duration such that the temporal derivative ($\partial \vec{u}/\partial t$) becomes very large compared to the spatial-derivative terms. Wood et al. (2000) state that this assumption is valid when the number ($t_d U/S$) is very small, where t_d is the impact duration, U is the impact velocity and S a length scale. In this paper we refer to this number as the Peregrine Number Λ considering the overhang length as the length scale, being $\Lambda = t_d U/W$. With the previous considerations, it is possible to approximate the equation of motion to Equation (3).

$$\frac{\partial \vec{u}}{\partial t} = -\frac{1}{\rho}\nabla p \tag{3}$$

where $\vec{u}$ [m/s] is the velocity vector, p [Pa] is the pressure and ρ [kg/m_3] is the fluid density.

Combining Equations (1) and (3), and considering continuity for an incompressible fluid, we observe that the pressure-impulse satisfies the Laplace equation ($\nabla^2 P = 0$). Together with the boundary conditions shown in Fig. 4 (in dimensionless form), this equation can be solved in

order to obtain the dimensionless pressure-impulse distribution in the desired domain and on the vertical wall.

In this paper, the pressure-impulse model is used in a dimensionless form. This is obtained considering the overhang length W (see Fig. 3) as the geometric scaling magnitude and making the impact area boundary condition also dimensionless (see Fig. 4). The geometric dimensions are made dimensionless as follows:

- The dimensionless overhang length $\overline{W}$ is equal to 1,
- the dimensionless overhang height $\overline{h}$ is equal to $h/\ W$, and
- the dimensionless axes are $\overline{x} = x/W$ and $\overline{z} = z/W$.

The impact area boundary condition is made dimensionless by the wave impact velocity (U) and the fluid density (ρ) as shown in Equation (4). The factor β was introduced by Wood et al. (2000) to describe the increase in impact pressure-impulse due to the bounce-back of entrapped air. An impact area fully covered by air would have $\beta = 2$ while an impact in vacuum would have a $\beta = 1$. In this paper β is used to account for all differences between theory and measurement, so we name it the effective bounce-back factor.

$$\frac{\partial \overline{P}}{\partial \overline{z}} = \beta \tag{4}$$

For the nondimensionalization and re-dimensionalisation of the results, the following conversion expressions are used for the pressure-impulse (P) obtained at any point in the fluid domain and for the total force-impulse (I) integrated over a given boundary such as the vertical structure below the overhang.

$$\overline{P} = \frac{P}{\rho U W} \tag{5}$$

$$\overline{I} = \frac{I}{\rho U W^2} \tag{6}$$

where ¯ represents dimensionless values, P [Pa·s] is the pressure-impulse obtained at any point in the fluid domain, I [N·s/m] is the total force-impulse integrated over a given boundary (e.g. vertical wall below overhang) for 1 m length, ρ [kg/m$_3$] is the fluid density, U [m/s] is the impact velocity and W [m] is the overhang length and the scaling factor.

2.2. Theoretical solution

This section presents the solution for the pressure-impulse theory, taking into account the nondimensionalization described previously and considering the configuration as shown in Fig. 4. This solution is based on that of Wood and Peregrine (1996), using the semi-analytical method. This semi-analytical solution resolves the pressure-impulse theory using conformal maps. The three domain transformations used in this solution are shown hereafter.

- Conformal map: $w = u + iv = \cosh(\pi y/\overline{h})$, being $y = x + iz$ the original plane in Fig. 4.
- Translation and magnification: $c = f + ig = Mw + N$, being $M = 2/(\cosh(\pi/\overline{h}) - 1)$ and $N = M + 1$.
- Conformal map. $\zeta = \xi + i\lambda = \overline{h}\cosh^{-1}(c)/\pi$, being ζ the plane where the solution is obtained.

Following these three transformations, and solving by separation of variables, the semi-analytical expressions for calculating the pressure-impulse are shown in Equations (7) and (8). This method is solved in this study considering $n = 30$ summations, after which convergence in the results is obtained.

$$\overline{P}_{\overline{x},\overline{z}} = \beta \sum_{n=1}^{30} a e^{-\alpha_n \xi} \cos(\alpha_n \lambda) \tag{7}$$

$$a = \frac{2}{\alpha_n \overline{h}} \int_0^{\overline{h}} \frac{1}{M} \frac{\sin(\pi\lambda/\overline{h})\cos(\alpha_n \lambda)}{\sqrt{b^2 - 1}} d\lambda \tag{8}$$

where $\overline{P}^n_{\overline{x},\overline{z}}$ is the dimensionless pressure-impulse at location $(\overline{x},\overline{z})$, $\alpha_n = (n + 1/2)/\pi$, $b = (\cos(\pi\lambda/\overline{h}) - N)/M$ and the additional parameters should be used as previously defined in this paper. Note that the original variables names have been modified for consistency in this study. Note also two corrections made from expressions from Wood and Peregrine, 1996, which are assumed to be typos in Wood and Peregrine, 1996 given that the results are in full agreement. First, the original variable a_m is used as equal to a_n, while A_m is used as equal to A_n. Secondly, the expression for b is corrected with the addition of $/\overline{h}$ inside the cosine parenthesis.

This semi-analytical solution is compared with a numerical solution for the same problem using a second order central differences relaxation scheme as given in Hofland et al., 2019, and a very high agreement is observed. The deviation for the total force-impulse on the wall is 0.3% for the shorter overhang, and 0.9% for the longer overhang. Given the much higher efficiency of the semi-analytic solution, this is the method that is used in this study. According to these calculations, the total force-impact on the wall ($\overline{I} = I/\rho U W^2$) is equal to 1.62β for the shorter overhang and 1.30β for the longer overhang.

2.3. Dimensionless pressure-impulse estimation

This section presents the graphs and expressions in order to estimate the dimensionless pressure-impulse and force-impulse of a wave impact. It addresses both the dimensionless local pressure-impulses ($\overline{P} = P/\rho U W$) and the dimensionless total force-impulses acting at the vertical wall ($\overline{I} = I/\rho U W^2$).

Fig. 5a shows (for $\beta = 1$) the dimensionless pressure-impulse profile for various dimensionless overhang heights $\overline{h}$, with a normalized overhang height $\overline{z}/\overline{h}$. The fully analytical solution for an infinite depth presented by Wood and Peregrine, 1996 is also plotted for a depth of $\overline{h} = 10$. Fig. 5b presents (for $\beta = 1$) the maximum and minimum dimensionless local pressure-impulse $\overline{P}$ calculated at the top ($\overline{z} = \overline{h}$) and the bottom ($\overline{z} = 0$) of the vertical wall respectively. Equations (9) and (10) give fits of the semi-analytical solution for the maximum and minimum pressure-impulse as function of overhang height, and for other values of β.

Fig. 6 shows (for $\beta = 1$) the dimensionless force-impulse on the vertical wall below the overhang ($\overline{I}$) for different dimensionless overhang heights $\overline{h}$. It is not known to the authors that the pressure-impulse theory has been used for this estimation of the total force-impulse at the vertical wall before, as it is introduced here. This force-impulse can be estimated for any value of dimensionless overhang heights $\overline{h}$ and effective bounce-back factor β according to the fit presented in Equation (11).

2.4. Impact velocity prediction

The wave impact velocity is required for obtaining the dimensional pressure-impulse from theoretical estimations, or for obtaining the dimensionless pressure-impulse from experimental measurements. For

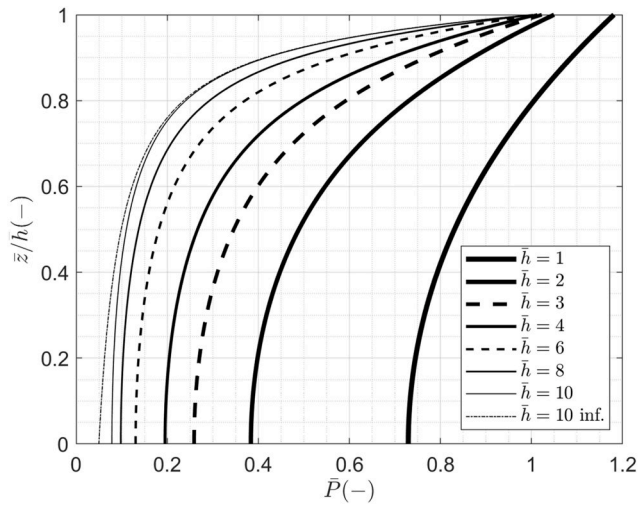

(a) Pressure-impulse profile at wall for $\beta = 1$.

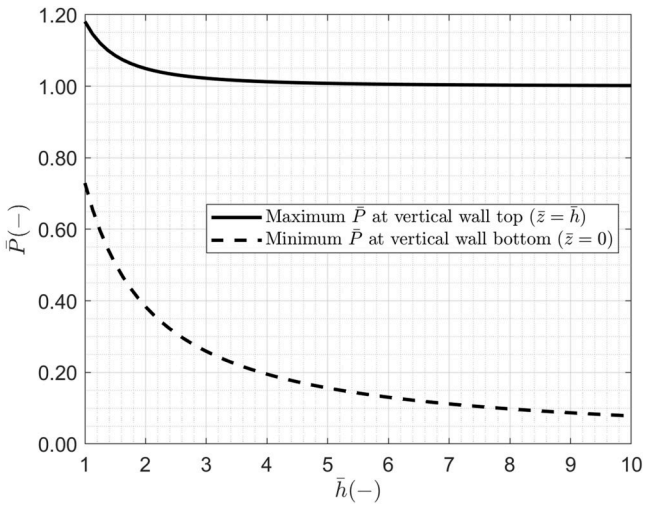

(b) Max and min pressure-impulse at wall for $\beta = 1$.

Fig. 5. Dimensionless pressure-impulse at wall ($\overline{P} = P/\rho UW$) for various $\overline{h}$ for $\beta = 1$.

$$\overline{P}_{max} = \beta\left(0.18\overline{h}^{-1.9} + 1\right) \text{for} 1 \le \overline{h} \le 10 \tag{9}$$

$$\overline{P}_{min} = \beta\left(0.75\overline{h}^{-0.97}\right) \text{for} 1 \le \overline{h} \le 10 \tag{10}$$

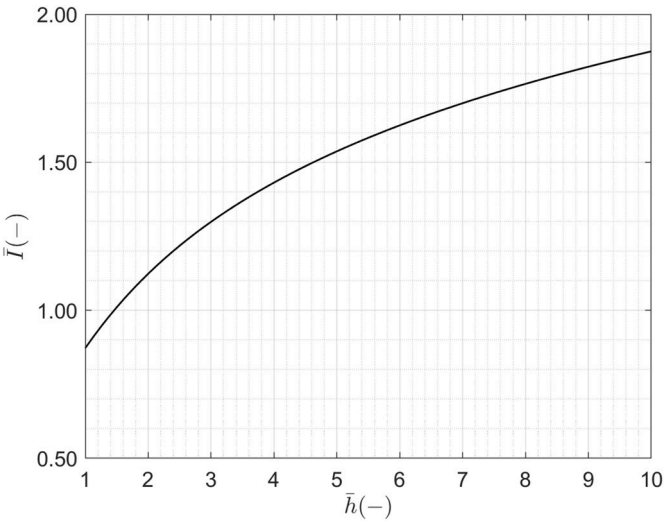

Fig. 6. Total dimensionless force-impulse at wall ($\bar{I} = I/\ \rho UW^2$) for $\beta = 1$.

$$\overline{I} = \beta\left(2\overline{h}^{0.18} - 1.14\right) \text{for} 1 \le \overline{h} \le 10 \tag{11}$$

predicting this impact velocity, an expression based on linear wave theory is used in this study. This theory is considered suitable for the waves used in this study (Hedges, 1995) and it is a well known theory that can be implemented in a simple way in future design methodologies. According to this theory, a linear wave reflecting against a vertical wall can be described as in Equation (12).

$$\eta = (1 + cr)\frac{H_i}{2}\sin\omega t = A_w \sin\omega t \tag{12}$$

where η is the surface elevation at the wall, cr is the wave reflection coefficient at the wall, H_i is the incident wave height, ω is the angular wave frequency ($\omega = 2\pi/T$, where T is the incident wave period) and A_w is the total wave amplitude at the wall.

Combining Equation (12) (water surface position) with its derivative (water surface velocity), the water surface velocity $\dot{\eta}$ can also be expressed as function of the water surface position η ($\dot{\eta} = \omega\sqrt{A_w^2 - \eta^2}$). Furthermore, this study considers the reflection coefficient as $cr = 1$, since the incident wave is not influenced by the overhang during the period $T/2$ before the wave impact occurs. The impact velocity (U) can then be obtained from Equation (13), for the condition of zero freeboard ($d = h$) considered in this study.

$$U = \omega H_i \tag{13}$$

3. Laboratory experiments

This section describes the experimental tests carried out in this study, including the experimental facility, the main characteristics of the setup configuration, the instrumentation used, how the pressure-impulses and force-impulses are estimated and a first overview of the measured results.

3.1. Facility

The experimental data used in this paper was obtained from two test campaigns (2018 and 2019) carried out at the wave flume at the Hydraulic Engineering Laboratory at the Delft University of Technology. Fig. 7a shows an overview of the test area, illustrating the impact structure (vertical structure with an overhang) inside the wave flume and connected to instrumentation and acquisition systems. Fig. 7b shows in more detail the aluminium overhang surface supported by a 920 kg concrete block during a wave impact. The use of this massive concrete block, solid aluminium profiles and 10 mm thick aluminium plates provided the stability and rigidity for the wave impact tests. The wave flume is 42 m long, 1 m high and 0.8 m wide. The wave generation equipment consists of a piston-type wave maker able to generate regular and irregular waves and is equipped with active reflection compensation (ARC) and second order wave steering.

(a) Experimental test area. (b) Overhang structure model setup.

Fig. 7. Overview of the experimental facility and model setup.

3.2. Experiment description

The test setup was built with an aluminium structure mounted on a concrete block inside the wave flume (see Fig. 7), with the vertical wall located at 23.3 m away from the wave generator paddle (30.8 m in the 2018 tests). The concrete block is 0.8 m wide, 0.8 m long and 1 m high and provides the stability for the structure subjected to wave impacts. The configurations considered in this study include a shorter overhang ($W = 0.1$ m) and a longer overhang ($W = 0.2$ m), as shown in the test setup illustration in Fig. 8. The regular incident waves considered in the tests are shown in Table 1. In total, 14 tests were carried out (seven for the shorter overhang and seven for the longer overhang): conditions A, B, C, D and E in 2019 and conditions A and F in 2018. For the two configurations and all incident wave conditions, the water level is located at the same height of the overhang ($d = h = 0.6$ m). These conditions are chosen because the vertically upwards moving wave surface is expected to have the maximum speed when impacting the overhang. This is expected to lead to the highest wave impact loading. For all the test conditions and configurations, 50 regular waves were considered, in order to obtain statistical information regarding the repeatability and variability of wave impact magnitudes for identical repeated incident wave conditions.

3.3. Instrumentation

An array of 3 wave gauges, with a sampling rate of 100 Hz, allowed to obtain the incident and reflected waves at 1.5 m away from the vertical wall, according to the method from Zelt and Skjelbreia (1992), see Fig. 8. All wave gauges were equipped with temperature compensation systems in order to ensure the accuracy of the water level measurements in all conditions during the tests.

Table 1
Experimental target wave conditions (see Appendix A - List of symbols).

Condition	H [m]	T [s]	L_0 [m]	s_0 [-]	h [m]	d [m]	Number of waves [-]
A	0.06	1.30	2.64	0.023	0.6	0.6	50
B	0.08	1.60	3.99	0.020	0.6	0.6	50
C	0.10	1.30	2.64	0.038	0.6	0.6	50
D	0.10	1.60	3.99	0.025	0.6	0.6	50
E	0.10	2.00	6.24	0.016	0.6	0.6	50
F	0.10	1.90	6.24	0.018	0.6	0.6	50

The results from 4 pressure sensors are analysed (6 in the 2018 tests). The pressure sensors used in the tests are Kulite HKM-375M-SG with 1 bar measurement range and sealed gauge. The sampling frequency was 20 kHz. The location of these pressure sensors is shown in Fig. 8. The pressure sensors PS2 and PS4 were only used in the 2018 tests. In all the analyses in this study, the used pressures/forces are the dynamic values, obtained once the hydrostatic pressures/forces (the pressures/forces measured before wave motion) are removed from the measurements.

Three Olympus Tough TG-5 cameras were used during the tests, with a frame rate of 59.94 fps and a resolution of 1920x1080. These camera recordings are synchronized with the pressure/wave measurements through LED light pulses recorded by the camera. In this study, only Camera 1 is used, which was located 0.5 m from the flume wall, and

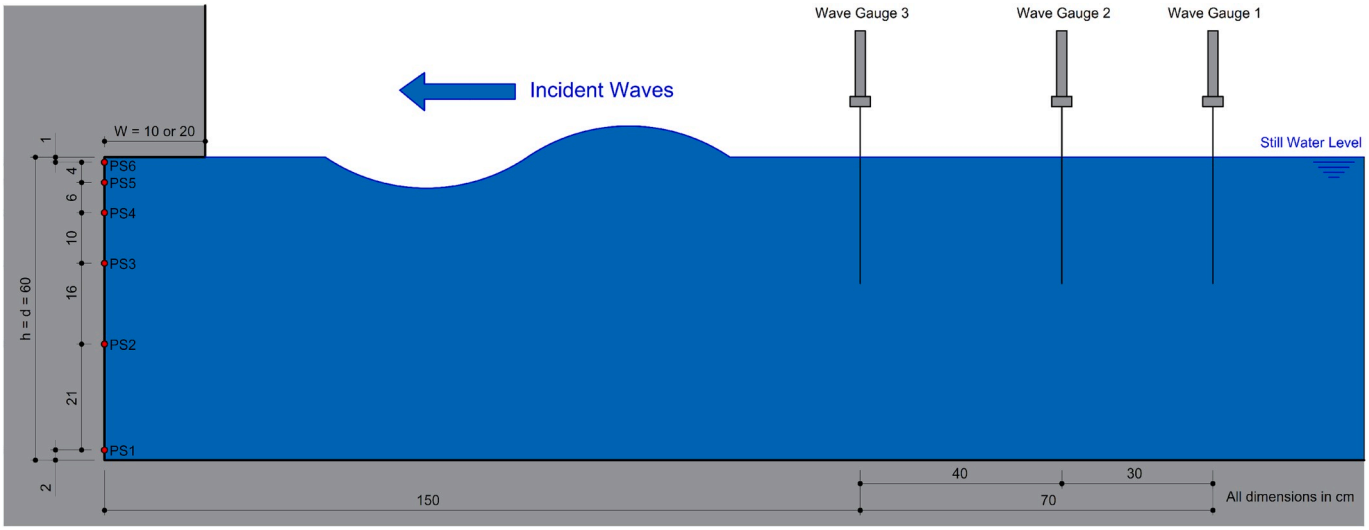

Fig. 8. Illustration of test setup and instrumentation. Note that all dimensions are in centimetres (cm).

slightly below the overhang height.

3.4. Experimental pressure-impulse calculation

This section describes the procedure used to estimate the pressure-impulses from the experimental results. Various methods were previously presented for obtaining the pressure-impulse (De Almeida et al., 2019; Cooker and Peregrine, 1990; Wood et al., 2000), but the large range of variations on the wave impact impulsive pressure signals leads to a lack of a unique method to objectively determine the pressure-impulse of different wave impacts. The method presented here addresses this issue as it follows a consistent procedure to objectively estimate pressure-impulses from the large range of different wave impact types observed in this study, with a constant criteria. This method is shown in Fig. 9 and described hereafter. The pressure-impulse is defined as the grey dashed area located between the impact start and the impact end. In this figure, the orange colours represent the impulsive part of the load while the blue ones represent the quasi-static part. The dashed blue line represents a low-pass filter applied to the impulsive time-series. In this method, the impact start is roughly defined when the pressure becomes larger than zero (i.e. hydrostatic pressure), and the impact end is roughly defined when the pressure becomes smaller than the quasi-static component.

This method is used for the analysis of the experimental results, as shown in the examples from Fig. 10. The measured impulsive pressure time-series was used after being filtered according to a low-pass third order Butterworth filter with a cut-off frequency of 100 Hz. This cut-off frequency was defined given that it allows to remove small higher frequency components but it is sufficiently large to not affect the pressure-impulse magnitude or the impact duration. Similarly, the quasi-static component was obtained after filtering the same measured pressure time-series with low-pass third order Butterworth filter with a cut-off frequency equal to two times the frequency of the incident waves. The impact start is obtained when the impulsive pressure time-series, black line, rises above 20% of the quasi-static peak, shown with the black dot. Further, the impact end is obtained when the impulsive pressure time-series, black line, approaches the quasi-static component, blue line, and their difference becomes smaller than 20% of the quasi-static peak, as shown with the magenta dot. For wave impacts with post-peak vibrations, the impact-end position is obtained after the pressure time-series, black line, is further filtered (with 25 Hz cut-off frequency), in order to limit the effect of post-impact vibrations on the estimation of the pressure-impulse and impact duration. Finally, the pressure-impulse

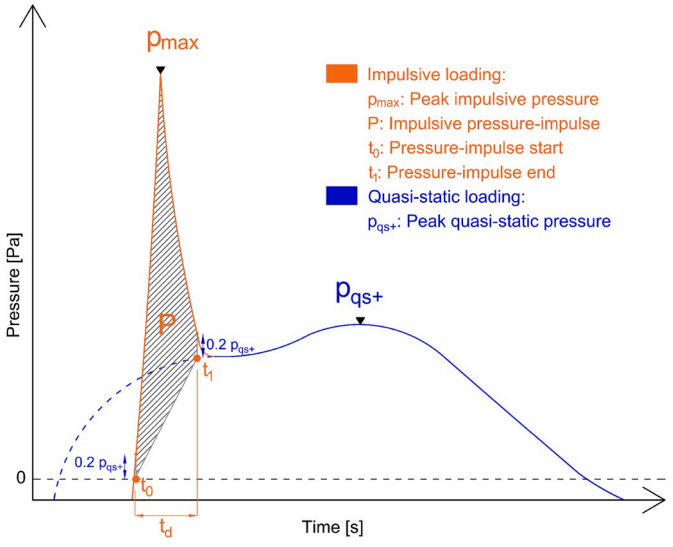

Fig. 9. Pressure-impulse calculation method.

is obtained as the integral of the area shown in green (see Fig. 10). This procedure is applied first at the uppermost location at the vertical wall (PS6, as shown in Fig. 10), which is the closest to the wave impact location and the one that shows the highest impulsive pressures. Thus, the impact duration measured at PS6 is used as the global impact duration for a given wave impact. For the other locations lower in the vertical wall (PS1 to PS5, see Fig. 8), an equivalent calculation is made based mainly on the impact durations defined at PS6. The impact start for PS1 to PS5 is equal to the impact start for PS6. Similarly, the impact end for PS1 to PS5 is equal to the impact end for PS6, but only if, and after, the difference between the impulsive pressure time-series and the quasi-static component is smaller than 20% of the peak impulsive pressure at that location, in order to capture accurately the complete pressure-impulse at those locations. The total force-impulse is then calculated by integrating the obtained pressure-impulse profile over the vertical wall height. For the validation of the theoretical model, the measured pressure-impulses are made dimensionless according to Equation (5) for $\overline{P}$ and Equation (6) for $\overline{I}$. In those equations, the wave impact velocity is obtained according to the linear wave theory expression shown in Equation (13).

3.5. Experimental results

This section presents a summary of the experimental results, with focus on the incident wave height characteristics, the pressure/forces measurements and the camera recordings. For decomposing the incident and reflected wave conditions, the method presented by Zelt and Skjelbreia (1992) was used. Table 2 summarizes the experimental results for the 14 tests, named according to the wave condition (see Table 1), the overhang dimension (S represents the shorter overhang with W = 0.1 m, while L represents the longer overhang with W = 0.2 m) and the year when the tests were carried out. It includes the mean incident wave height (H), the variability of the incident wave height (σ_H/μ_H), the mean wave period (T), the mean wave length (L), the mean steepness (s), the reflection coefficient (c_r) and the Ursell Number ($U_r = HL^2/d^3$) as a measure of the wave field non-linearities. According to Hedges, 1995 and considering the range of Ursell Number in all tests (1.6–9.0), and the ratios of H/L (0.02–0.04), d/L (0.14–0.25) and H/d (0.10–0.18), this wave field can be described theoretically by linear wave theories, as it is done in this study. Fig. 11 presents two examples of incident wave time-series, for condition A (smaller shorter waves, Fig. 11a) and for condition E (higher longer waves, Fig. 11b). For all test conditions, the incident wave for tests with overhangs presented reduced deviations when compared with additional tests carried out with a vertical wall without an overhang. The average deviation in incident wave height is 3.7% (3.0% for short overhangs and 4.5% for long overhangs), when comparing tests with and without overhangs exposed to the same wave generation signal. In the tests without overhangs, the measured total wave height at the vertical wall (H_{tot}) was compared with the assumed total wave height from the incident wave height ($H_{tot} = 2H_i$), leading to an average difference of 1.1%.

Table 2 includes also the mean impact durations (t_d), the calculated impact velocity (U) according to Equation (13) and the Peregrine Number ($\Lambda = t_d U/W$), similar to the one introduced by Wood et al., 2000 that describes the validity of the pressure-impulse theory. Given the small values of Λ ($\Lambda \ll 1$) it is plausible that the wave impacts considered in this study can be described theoretically by the pressure-impulse theory. Furthermore, Table 2 also includes for each test the mean dimensionless force-impulse ($\overline{I}$), the variability of the dimensionless force-impulse ($\sigma_{\overline{I}}/\mu_{\overline{I}}$) and the effective bounce-back factor (β).

Fig. 10 presents the six wave impact types observed during the tests. These figures display the pressure time-series for the pressure sensors at the highest position at the vertical wall (PS6), including the pressure peaks, impact start point, impact end point and the estimated impact-

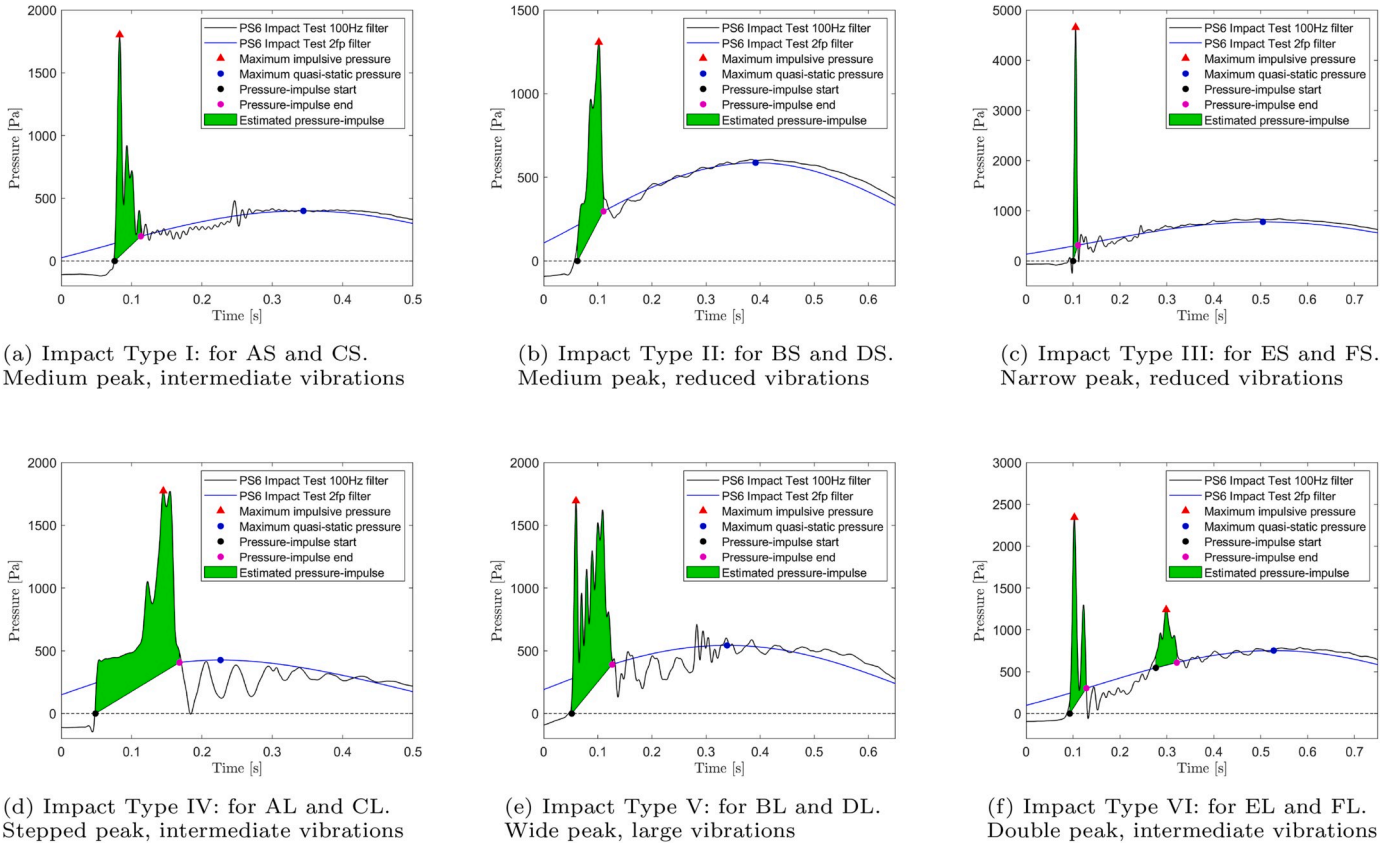

(a) Impact Type I: for AS and CS. Medium peak, intermediate vibrations

(b) Impact Type II: for BS and DS. Medium peak, reduced vibrations

(c) Impact Type III: for ES and FS. Narrow peak, reduced vibrations

(d) Impact Type IV: for AL and CL. Stepped peak, intermediate vibrations

(e) Impact Type V: for BL and DL. Wide peak, large vibrations

(f) Impact Type VI: for EL and FL. Double peak, intermediate vibrations

Fig. 10. Recorded pressure peaks for various wave impact types, at the highest location in the vertical wall (PS6), with coloured areas representing pressure-impulse (P). Note that axis scales differ.

Table 2
Summary of experimental results (see Appendix A - List of symbols).

Test	W [m]	H [m]	$\frac{\sigma_H}{\mu_H}$ [%]	T [s]	L [m]	s [-]	c_r [-]	U_r [-]	t_d [ms]	U [$\frac{m}{s}$]	Λ [-]	$\bar{I}$ [-]	$\frac{\sigma_{\bar{I}}}{\mu_{\bar{I}}}$ [%]	β [-]
AS19	0.1	0.061	2.3	1.30	2.42	0.025	0.84	1.7	37	0.294	0.11	1.68	4.6	1.04
BS19	0.1	0.084	1.8	1.60	3.27	0.026	0.93	4.1	52	0.328	0.17	1.78	4.3	1.10
CS19	0.1	0.103	3.7	1.31	2.43	0.042	0.81	2.8	36	0.497	0.18	2.19	6.2	1.35
DS19	0.1	0.104	2.4	1.60	3.27	0.032	0.94	5.2	42	0.409	0.17	2.00	6.2	1.23
ES19	0.1	0.101	0.4	2.00	4.36	0.023	0.92	8.9	10	0.318	0.03	1.68	7.5	1.03
AS18	0.1	0.059	1.4	1.30	2.42	0.024	0.85	1.6	40	0.283	0.11	1.76	4.8	1.08
FS18	0.1	0.099	1.1	1.90	4.09	0.024	0.99	7.7	14	0.329	0.05	1.88	5.8	1.15
AL19	0.2	0.060	1.3	1.30	2.42	0.025	0.67	1.6	110	0.288	0.16	1.43	3.3	1.10
BL19	0.2	0.085	3.1	1.60	3.27	0.026	0.78	4.2	69	0.335	0.11	1.55	3.7	1.19
CL19	0.2	0.100	2.0	1.30	2.43	0.041	0.63	2.7	101	0.483	0.24	1.76	3.5	1.36
DL19	0.2	0.108	3.5	1.60	3.27	0.033	0.74	5.4	57	0.426	0.12	1.62	7.0	1.25
EL19	0.2	0.103	0.6	2.00	4.36	0.024	0.82	9.0	37	0.323	0.06	1.67	9.1	1.29
AL18	0.2	0.059	1.2	1.30	2.42	0.024	0.69	1.6	116	0.286	0.17	1.38	3.4	1.06
FL18	0.2	0.105	1.7	1.90	4.09	0.026	0.82	8.1	54	0.347	0.09	1.46	10.4	1.12

related pressure-impulse. Impact Type I is observed in the tests AS and CS, characterized by one peak, an intermediate level of vibrations and an intermediate impact duration. Impact Type II is observed in the tests BS and DS, characterized by one peak, almost no vibrations and an intermediate impact duration. Impact Type III is observed in the tests ES and FS, characterized by one peak, a reduced level of vibrations and a very short impact duration. Impact Type IV is observed in the tests AL and CL, characterized by one stepped wide peak, an intermediate level of low-frequency vibrations and a very long impact duration. Impact Type V is observed in the tests BL and DL, characterized by one peak with a close secondary peak, large vibrations and a long impact duration. Impact Type VI is observed in the tests EL and FL, characterized by two peaks with an interval of 0.2 s ($\approx T/10$) between them, an intermediate level of vibrations and an intermediate impact duration. For wave impact Type VI, the impact duration (t_d) in Table 2 represents the duration of the first impact.

Fig. 12 illustrates the six wave impact types, with camera recordings at the moment when the water surface is seen to impact the overhang. Six different wave impact patterns are observed, with distinct wave shapes and air entrapments, both of which are considered to be related to each other. Thus, it can be expected that, although in different ways in each test, this entrapped air (but possibly also less extensive entrained air) plays a role in the measured wave impact loads on the structure. Furthermore, it was observed that a singular impact occurs for wave impact Type VI (conditions EL and FL), where external part of the overhang (first peak in Fig. 10f), followed by a second impact on the left inner side of the overhang (second peak in Fig. 10f).

The experimental results show that in all the tests air is entrapped

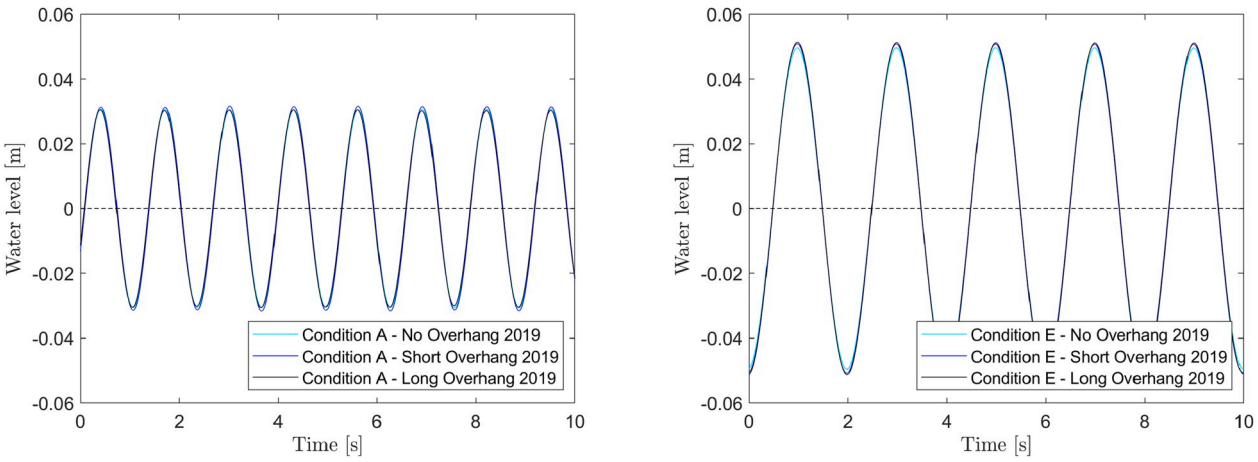

(a) Smaller shorter waves - Condition A.

(b) Higher longer waves - Condition E.

Fig. 11. Example of incident wave time series measured at 1.5 m from the vertical wall.

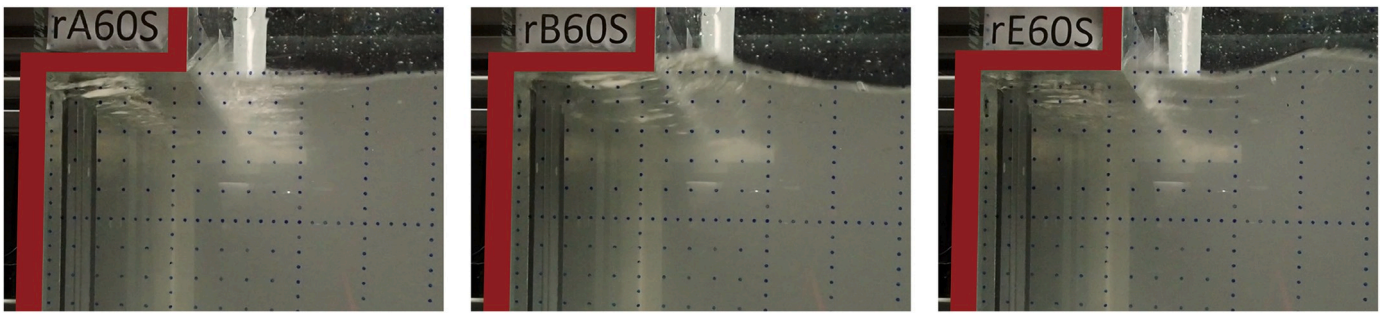

(a) Impact Type I: for AS and CS. Intermediate entrapped air, near the wall

(b) Impact Type II: for BS and DS. Intermediate entrapped air, distributed

(c) Impact Type III: for ES and FS. Reduced entrapped air, distributed

(d) Impact Type IV: for AL and CL. Extensive entrapped air, distributed

(e) Impact Type V: for BL and DL. Intermediate entrapped air, far from wall

(f) Impact Type VI: for EL and FL. Double peak, singular air pattern

Fig. 12. Impact types, from camera recordings at the moment when the water surface impacts the overhang. For wave impact Type VI, Fig. 12f displays the moment of the first impact, corresponding to the first pressure peak shown in Fig. 10f.

during the wave impact. In the tests with larger air entrapment, such as Impact Type IV, the impact duration was much longer. In the tests with smaller air entrapment, such as Impact Type III, the impact duration was much shorter, and the pressure peak was remarkably higher. Furthermore, a comparison between wave impact Type II (medium peak) and Type III (narrow high peak) is carried out, both of which have the same overhang length and relatively similar incident waves. This comparison (considering the examples shown in Fig. 10b and c) shows a very large difference in peak pressures (356%) while the difference in the pressure-impulse (P) is much smaller and negative (−6.47%). In summary, the experimental tests in this study indicate that an increased presence of air in wave impacts leads to a larger variability of wave impact magnitudes, a slight increase in the impulses, a large increase in the impact durations and a large decrease of the pressure/force peaks.

4. Validation of the theoretical model

This section addresses the validation of the theoretical model presented in Section 2, with the experimental results described in Section 3. The long waves considered in this study ($L \gg W$) are used to theoretically have a uniform impact velocity over the length of the overhang, in agreement with how it is considered in the pressure-impulse theory schematization (see Section 2). All the tests used in this study were carried out with regular waves and the following ranges of

dimensionless ratios.

- d/H: between 5.6 and 10.2
- W/H: between 0.96 and 3.38
- L/W: between 12.1 and 43.6
- h/W: 3 and 6
- $\Lambda = t_d U/W$: between 0.05 and 0.24

4.1. Pressure-impulse profile $\overline{P}$

This section addresses the pressure-impulse profile at the vertical wall ($\overline{P}$) caused by a standing regular wave impact. Fig. 13 shows the theoretical formulae compared with the experimental results for all the tests carried out. In the graphs from Fig. 13, the solid line represents the dimensionless pressure-impulse profile on the vertical wall based on the pressure-impulse theory for $\beta = 1$. The black dots represent the dimensionless pressure-impulse measured from the laboratory tests, obtained as the mean of the 50 regular waves used in the analysis of each test. From these results, the dashed line represents the experimental pressure-impulse profile, obtained as a power fit from to the measured data. In addition, from the analysis of the 50 waves from each test, a 95% confidence band for the mean ($\delta = \pm 2.009\sigma\sqrt{1/50}$) and a 95% prediction interval for a separate observation ($\delta = \pm 2.009\sigma\sqrt{1+1/50}$) are shown, calculated according to the student-t distribution. In order to make the measured pressure-impulse dimensionless, the impact velocity according to Equation (13) is used, considering the measured incident wave data from Table 2.

According to the graphs in Fig. 13, the experimental results showed good agreement with the theoretical estimations. In all the cases, the shape of the vertical distribution is in agreement, with a general underestimation by pressure-impulse predictions with the theoretical no air effect ($\beta = 1$). The total force-impulse estimations of the 14 tests are summarized in the last three columns in Table 2. For each of the tests shown in Fig. 13, the total force-impulse ($\bar{I}$) is calculated as the integral of the power fit profile (dashed line in Fig. 13) over the overhang height. Table 2 includes the measured mean values of the total force-impulse at the vertical wall ($\bar{I}$), the mean variations of the measured force-impulses from the 50 waves in a test ($\sigma_{\bar{I}}/\mu_{\bar{I}}$) and the calculated experimental effective bounce-back factor (β) for each test. These experiential results showed that the averaged mean variability of the total force-impulses ($\langle\sigma_{\bar{I}}/\mu_{\bar{I}}\rangle_{mean} = \langle\sigma_I/\mu_I\rangle_{mean} = 5.7\%$) is smaller than that of the total force peaks ($\langle\sigma_F/\mu_F\rangle_{mean} = 11.4\%$).

4.2. Total force-impulse at wall $\bar{I}$

In this section, the total force-impulse at the vertical wall $\bar{I}$ caused by a standing regular wave impact is analysed. The validation of the theoretical model is made based on regular wave experimental data, which were analysed individually in the previous section. Fig. 14 shows the experimental results (see Table 2) compared with the theoretical formulae.

These results show the suitability of the theoretical model based on the pressure-impulse theory for preliminary estimations of wave impact loading on vertical structures with overhangs. Fig. 14 (and also Table 2) shows that the measured force-impulses from the experimental tests are always higher than the theoretical estimations without the influence of air ($\beta = 1$). The experimental data in this study presents a mean value of $\beta = 1.17$ with a standard deviation of $\sigma_\beta = 0.11$, showing a relatively reduced deviation ($\sigma_\beta/\beta = 9.4\%$). Fig. 14 also shows the theoretical formulae with maximum bounce-back air effect ($\beta = 2$) according to pressure-impulse theory (Wood et al., 2000). According to this, the impact surface extension fully covered by an air bubble leads to a double pressure-impulse magnitude. Thus, the measured impulses above the no-air ($\beta = 1$) theoretical solution are in agreement with the camera recording from Fig. 12 where in all the tests a portion of impact surface below the overhang was covered by an air bubble with varying dimensions. It is remarkable that the impacts in test ES (Fig. 10c) lead to an impulse very close to the no-air theoretical solution ($\beta = 1$) while in Fig. 12c it can be seen that indeed only a small portion of air is entrapped at the moment of impact.

Fig. 15 combines all the pressure-impulse ($\overline{P}$) results from shorter overhang (Fig. 15a) and longer overhangs (Fig. 15b). The measured pressure-impulses (black dots) are combined with a power fitting of these combined measured results (dashed line), the no-air model estimation with $\beta = 1$ and the experimentally calibrated model estimation with $\beta = 1.17$. The model estimation with $\beta = 1.17$ is able to predict accurately the total force-impact on the wall ($\bar{I}$) as shown previously, but it underestimates the pressure-impulse at the lower part of the wall, while overestimates the pressure-impulse at the upper part of the wall. Furthermore, and especially for longer overhangs, the variability on the pressure-impulse at the upper part of the wall is remarkably higher. These differences observed at the upper part of the wall are expected to be caused by highly dynamic processes that take place during the wave impacts, and deviate partially from the assumptions of the pressure-impulse theory.

For estimating force-impulses from a wave impact (I), the following steps could be followed. First, the dimensionless overhang height $\overline{h} = h/W$ should be obtained from a given structure geometry. Second, the dimensionless force-impulse $\bar{I}$ can be obtained from Equation (11), using $\beta = 1.17$. Third, the wave impact velocity can be obtained from linear wave theory (see Equation (13), for $d = h$ and 100% wave reflection). And fourth, the dimensional force-impulse I can be estimated according to Equation (5). More extensive validation data is recommended in order to use this theoretical model as a design tool, including broader incident wave conditions and structure configurations.

5. Discussion

This section discusses the potential causes for differences between theory and measurements, which possibly are the suitability of the impact velocity estimation based on linear wave theory (U), the impulsive character of the wave impact assumed by the pressure-impulse theory (Λ), the influence of the air and other wave impact processes on the pressure-impulses (β) and the uncertainty regarding the method for obtaining the pressure-impulse (summarized in Fig. 9).

According to the data presented in Table 2 and the criteria from Hedges, 1995, the incident wave field can be described by the linear wave theories as used in this study. Furthermore, the additional tests carried out without an overhang showed that the measured total wave height at the wall and the vertical velocities were in agreement with the linear wave theory (3.2% discrepancy). Thus, it is concluded that the linear wave theory is suitable for describing the wave field in this study, and in consequence is suitable for the estimations of the wave impact velocity U, as presented in Equation (5). Furthermore, the simplicity of its expressions makes it particularly suitable for being used for a design estimation. The influence of the overhang on the kinematics near the structure should be accounted for, but the impact follows half a wave period ($T/2$) without the influence of the overhang on the incident wave. It is thus considered that the assumption of a 100% reflection ($cr = 1$) considered in this study is also valid.

Considering the data presented in Table 2 and the criteria from Wood et al., 2000, all the wave impacts in this study can be described by the pressure-impulse theory. The limited obtained values of Λ ($\Lambda = 0.05\text{to}0.24 < 1$) indicate that the assumptions made in the derivation of this theory (see Section 2) can be considered valid. The tests carried out in Wood et al., 2000 for breaking waves lead to values of Λ (considering the wave impact length as the length scale) between 0.14 and 0.40, which were also considered to be within the limits of the pressure-impulse theory validity. Nevertheless, it is also highlighted that

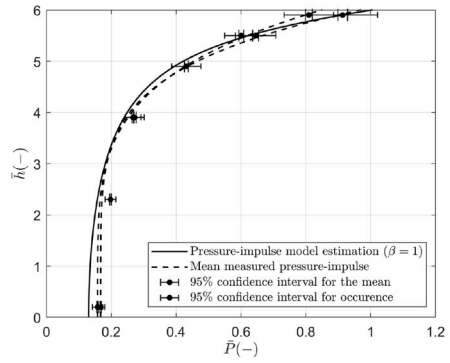

(I-AS) Type I, Condition AS.

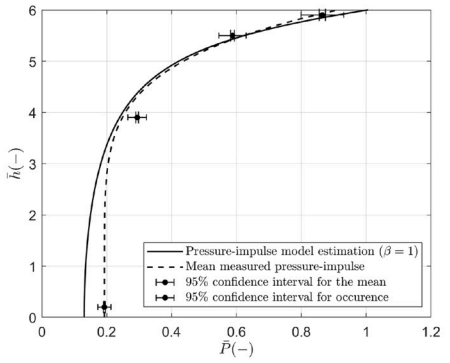

(II-BS) Type II, Condition BS.

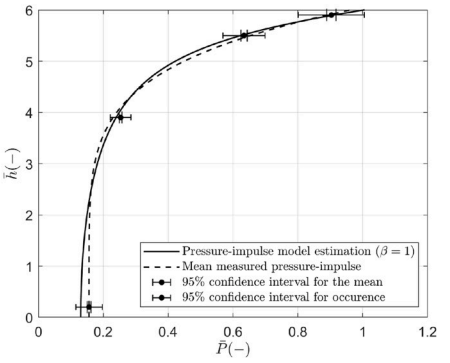

(III-ES) Type III, Condition ES.

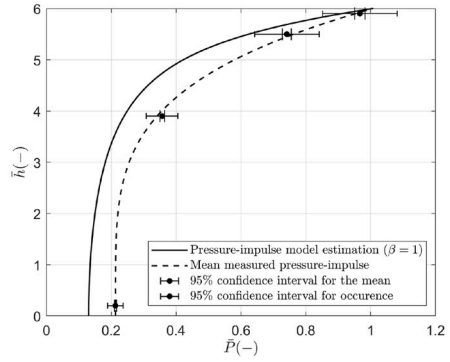

(I-CS) Type I, Condition CS.

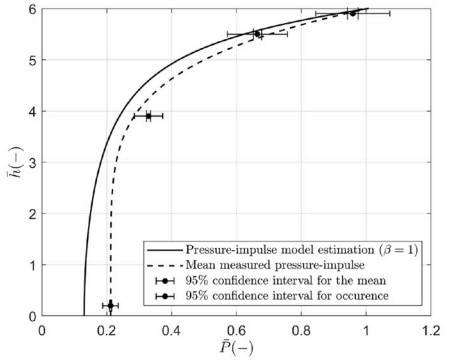

(II-DS) Type II, Condition DS.

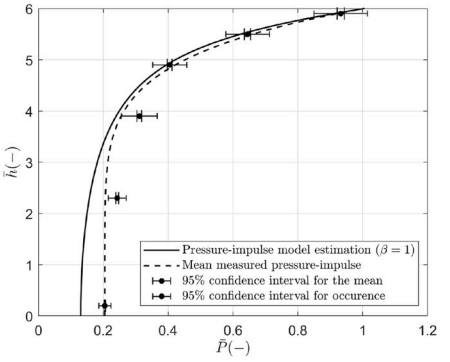

(III-FS) Type III, Condition FS.

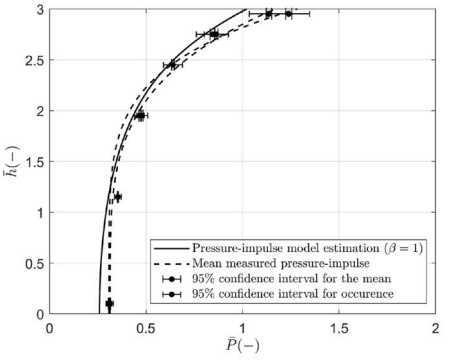

(IV-AL) Type IV, Condition AL.

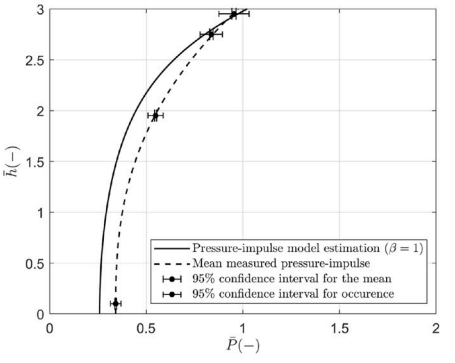

(V-BL) Type V, Condition BL.

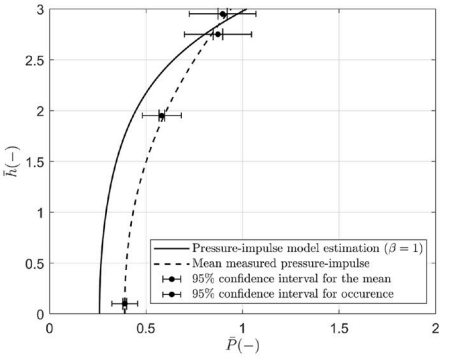

(VI-EL) Type VI, Condition EL.

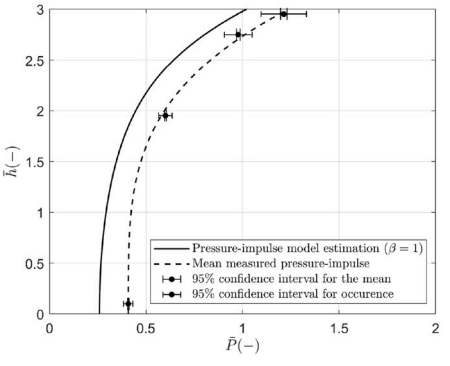

(IV-CL) Type IV, Condition CL.

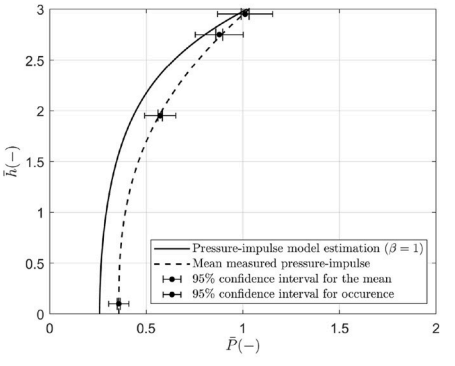

(V-DL) Type V, Condition DL.

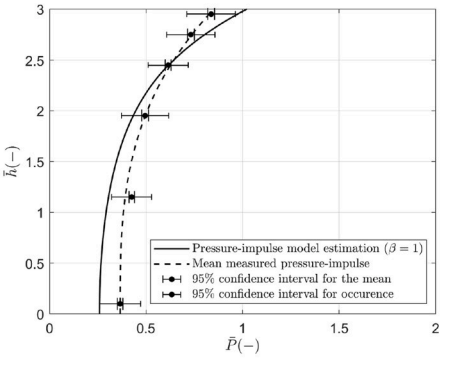

(VI-FL) Type VI, Condition FL.

Fig. 13. Dimensionless pressure-impulse profile $\overline{P}$. Note that axis scales differ.

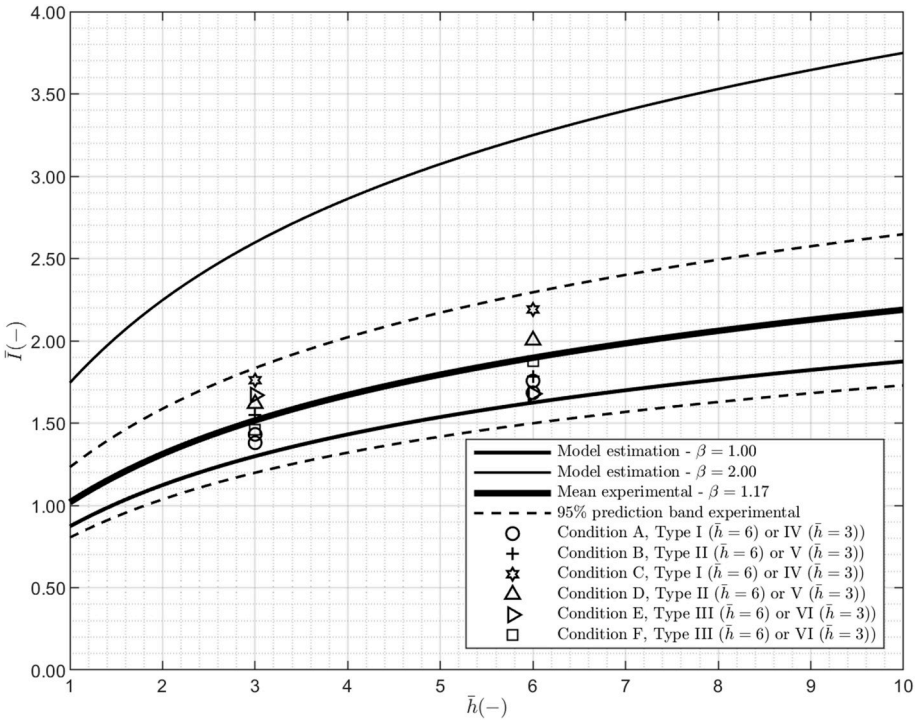

Fig. 14. Regular waves - Total dimensionless force-impulse at wall $\bar{I}$.

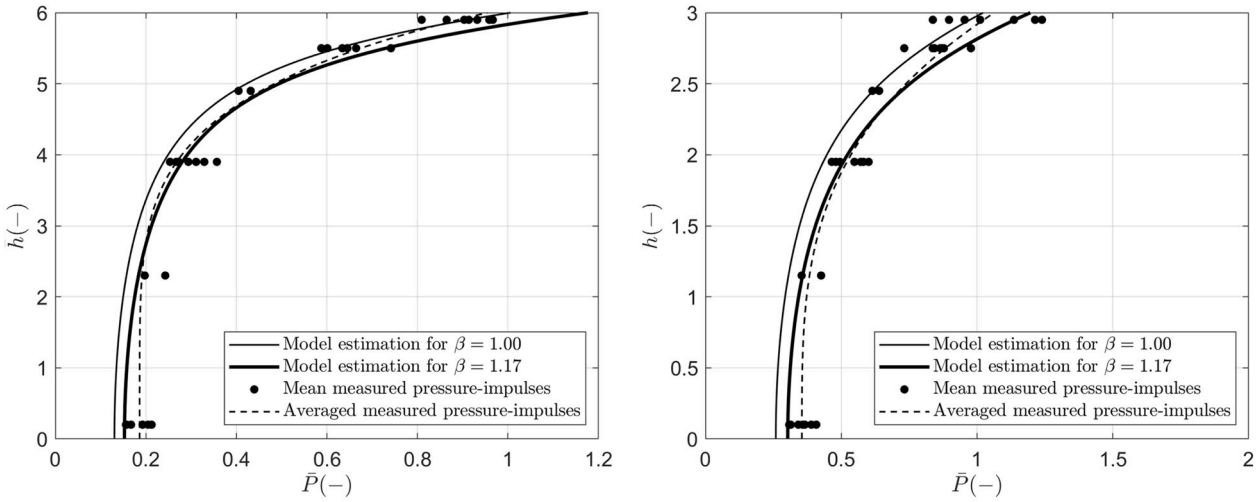

(a) Shorter overhang, all conditions.

(b) Longer overhang, all conditions.

Fig. 15. Summary dimensionless pressure-impulse profile $\bar{P}$.

more violent impacts with lower Λ are expected to show better agreement with the theory. Thus, although the test CL present a higher value of Λ, it is considered that all the tests in this study fall within the range of validity for the pressure-impulse theory.

Taking into account the observations from Fig. 12, the presence of vibrations in the time series from Fig. 10, the variation in pressure peaks and the variations in impact duration, it is concluded that the results of this study are influenced by the distinct presence of air in the various tests. It is also highlighted how the measured pressure-impulse from tests with a reduced amount of entrapped air at the impact (ES), is very similar to the theoretical estimations for no-air conditions ($\beta = 1$). In general, it is observed that a large air entrapment seems to be the main common factor for tests where $\beta \gg 1$. Thus, the factor β accounts in this study mainly for the presence of air in the impacts and the consequent deviations from the theoretical results with no air presence.

This study presents a method for the estimation of the pressure-impulse from the pressure measurements. This method follows other proposals from (De Almeida et al., 2019; Cooker and Peregrine, 1990; Wood et al., 2000), which do not define a consistent procedure to estimate the pressure-impulse of different impulsive pressure signals from different wave impact types. The method used in this study addresses this issue and provides a consistent criteria to calculate pressure-impulses in all tests in this study, including all different impulsive pressure signals. Thus, this method allows to limit the variability of pressure-impulse estimations based on varying estimation criteria. Nevertheless, this method should be further evaluated in a wider range of impulsive pressure time series.

6. Conclusions

The use of the pressure-impulse theory for estimating wave impact load magnitudes caused by standing regular waves on vertical structures with relatively short overhangs is evaluated. The theory is compared to laboratory experimental data, and a simplified but realistic configuration with regular waves was used to this end. This addresses an existing knowledge gap on wave impact loading estimations on such structures, since such an experimental validation of the pressure-impulse theory is not known to the authors. The aim of this paper is thus to contribute to the assessment of new and renovated coastal hydraulic structures with overhangs. The experimental data used in this study included relatively short overhangs with respect to the overhang height ($3 < h/\ W < 6$), relatively short overhangs with respect to the wave length ($12.1 < L/\ W < 43.6$), low steepness regular waves ($0.023 < s < 0.042$) and non-breaking conditions ($5.6 < d/H < 10.2$).

A model for estimating the pressure-impulse field caused by standing wave impacts on structures with overhangs based on the pressure-impulse theory is used. This allows to determine the pressure-impulse profile at the vertical wall below the overhang (P), and the total force-impulse (I) acting in such a vertical wall. The theoretical estimations are validated with experimental data, from which an effective bounce-back factor of $\beta = 1.17$ is obtained ($\sigma_\beta = 0.11$), accounting mainly for the effect of the air in the wave impact. The assumptions considered in the pressure-impulse theory are verified in this study, as the measured values of the newly named Peregrine Number ($\Lambda = t_d U/\ W$) are sufficiently small ($\Lambda = 0.05\text{to}0.24 < 1$). Furthermore, the wave impact velocity is estimated by linear wave theory ($U = \omega H_i$), for the condition of 100% reflection ($cr = 1$) and the zero freeboard used in this study. The use of a linear wave theory is supported, among others, by the reduced non-linearities of the incident waves as described by the Ursell Number ($1.6 < U_r < 9.0$) and the low steepness of the incident waves ($0.023 < s < 0.042$).

The analysis of the experimental data reinforces the previous observations that the pressure-impulses and force-impulses are more constant than pressure/force peaks. In this study the measured force-impulses are more stable ($\langle \sigma_{\bar{I}}/\mu_{\bar{I}} \rangle_{mean} = \langle \sigma_I/\mu_I \rangle_{mean} = 5.7\%$) compared with the force peaks ($\langle \sigma_F/\mu_F \rangle_{mean} = 11.4\%$), for tests consisting of 50 regular incident waves. Furthermore, a comparison between wave impact Type II (medium peak) and Type III (narrow high peak) is carried out, both of which have the same overhang length and relatively similar incident waves. This comparison shows a very large difference in peak pressures (356%) while the difference in the measured pressure-impulse (P) is much smaller and negative (−6.47%). This lower variability of pressure-impulses and force-impulses is regarded as a positive factor to recommend its use in the design of hydraulic structures. The theoretical model presented in this study can be used to this end, in order to estimate pressure-impulses and force-impulses from standing wave impacts on structures with relatively short overhangs. Nevertheless, more extensive validation of this method is recommended, accounting for a more extensive range of structure configurations and incident wave conditions.

Author Statement

E.d.A.: Conceptualization, Methodology, Validation, Investigation, Software, Writing-Review & Editing, Formal Analysis, Data Curation, Writing-Original Draft and Visualization.

B.H.: Conceptualization, Methodology, Validation, Investigation, Software, Writing-Review & Editing, Resources, Supervision, Funding Acquisition and Project Administration.

Declaration of competing interest

The authors declare that they have no known competing financial interests or personal relationships that could have appeared to influence the work reported in this paper.

Acknowledgements

This study is part of the DynaHicS (Dynamics of Hydraulic Structures) research programme, supported by NWO (Nederlandse Organisatie voor Wetenschappelijk Onderzoek) grant ALWTW.2016.041.

List of symbols

A_w	Total wave amplitude at wall [m]
c_r	Wave reflection coefficient [-]
D	Still water depth [m]
DLF_I	Structure dynamic load factor [-]
F	Force [N]
$F_{tot,r}$	Total reaction force [N]
F_{qs+}	Quasi-static force [N]
H	Overhang height [m]
$\bar{h}$	Dimensionless overhang height [-]
H	Wave height [m]
H_i	Incident wave height [m]
I	Force-impulse [N · s]
$\bar{I}$	Dimensionless force-impulse [-]
I_{im}	Total impulsive force-impulse [N · s]
L	Wave length [m]
L_0	Deep water wave length [m]
P	Pressure [Pa]
$p(x,t)$	Pressure time-series during impact i at location x [Pa]
P	Pressure-impulse [Pa · s]
$\bar{P}$	Dimensionless pressure-impulse [-]
$P(x)_i$	Pressure-impulse from impact i at location x [Pa · s]
S	Wave steepness [-]
s_0	Deep water wave steepness [-]
T	Wave period [s]

T_n	Structure natural period [s]
t_d	Wave impact duration [s]
t_0	Start of wave impact i [s]
t_1	End of wave impact i [s]
U	Impact velocity [m/s]
U_r	Ursell Number [-]
$\overrightarrow{u}$	Velocity vector [m/s]
X	Horizontal dimension [m]
$\overline{x}$	Dimensionless horizontal dimension [-]
W	Overhang length [m]
$\overline{W}$	Dimensionless overhang length [-]
Z	Vertical dimension [m]
$\overline{z}$	Dimensionless vertical dimension [-]
B	Effective bounce-back effect [-]
H	Wave surface position [m]
$\dot{\eta}$	Wave surface velocity [m/s]
Λ	Peregrine Number [-]
μ_F	Mean force [N]
μ_H	Mean wave height [m]
$\mu_{\overline{I}}$	Mean dimensionless force-impulse [-]
σ_β	Standard deviation of effective bounce-back effect [-]
σ_F	Standard deviation of force [N]
σ_H	Standard deviation of wave height [m]
$\sigma_{\overline{I}}$	Standard deviation of dimensionless force-impulse [-]
Ω	Angular wave frequency [s^{-1}]
ω_n	Angular structure natural frequency [s^{-1}]
ρ	Fluid density [kg/m^3]

References

Bagnold, R.A., 1939. Wave-pressure Research, vol. 12. The institution of Civil Engineers, pp. 202–226.

Bredmose, H., Peregrine, D., Bullock, G., 2009. Violent breaking wave impacts. part 2: modelling the effect of air. J. Fluid Mech. 641, 389–430.

Castellino, M., Sammarco, P., Romano, A., Martinelli, L., Ruol, P., Franco, L., Girolamo, P.D., 2018. Large impulsive forces on recurved parapets under non-breaking waves. a numerical study. Coast Eng. 136, 1–15.

Chen, X., Hofland, B., Altomare, C., Suzuki, T., Uijttewaal, W., 2015. Forces on a vertical wall on a dike crest due to overtopping flow. Coast Eng. 95, 94–104.

Chen, X., Hofland, B., Uijttewaal, W., 2016. Maximum overtopping forces on a dike-mounted wall with a shallow foreshore. Coast Eng. 116, 89–102.

Chen, X., Hofland, B., Molenaar, W., Capel, A., Gent, M.R.V., 2019. Use of impulses to determine the reaction force of a hydraulic structure with an overhang due to wave impact. Coast Eng. 147, 75–88.

Cooker, M.J., Peregrine, D.H., 1990. A model for breaking wave impact pressures. In: Proc. Coastal Engineering Conference 1990, Delft, The Netherlands.

Cooker, M.J., Peregrine, D.H., 1995. Pressure-impulse theory for liquid impact problems. J. Fluid Mech. 297, 193–214.

Cuomo, G., Allsop, W., Bruce, T., Pearson, J., 2010. Breaking wave loads at vertical seawalls and breakwaters. Coast Eng. 57 (4), 424–439.

De Almeida, E., Hofland, B., Jonkman, S., 2019. Wave impact pressure-impulse on vertical structures with overhangs. In: Proc. Coastal Structures Conference 2019, Hannover, Germany. Bundesanstalt für Wasserbau.

Dias, F., Ghidaglia, J.-M., 2018. Slamming: recent progress in the evaluation of impact pressures. Annu. Rev. Fluid Mech. 50 (1), 243–273.

Goda, Y., 1974. A new method of wave pressure calculation for the design of composite breakwater. In: Proc. Coastal Engineering Conference 1974, Copenhagen, Denmark.

Hedges, T., 1995. Regions of validity of analytical wave theories. In: Proc. ICE Water Maritime and Energy 1995, London, United Kingdom.

Herterich, J., Cox, R., Dias, F., 2018. How does wave impact generate large boulders? modelling hydraulic fracture of cliffs and shore platforms. Mar. Geol. 399, 34–46.

Hofland, B., 2015. Modeltesten Golfkrachten Spuisluizen Afsluitdijk, Meetrapport 1220263. Deltares, Delft, The Netherlands.

Hofland, B., Passos, M., De Almeida, E., 2019. Effect of venting holes to relieve wave impact pressures on flood gates with overhangs. In: Proc. Coastal Structures Conference 2019, Hannover, Germany. Bundesanstalt für Wasserbau.

Kisacik, D., Troch, P., Bogaert, P.V., Caspeele, R., 2014. Investigation of uplift impact forces on a vertical wall with an overhanging horizontal cantilever slab. Coast Eng. 90, 12–22.

Martinelli, L., Ruol, P., Volpato, M., Favaretto, C., Castellino, M., Girolamo, P.D., Franco, L., Romano, A., Sammarco, P., 2018. Experimental investigation on non-breaking wave forces and overtopping at the recurved parapets of vertical breakwaters. Coast Eng. 141, 52–67.

Minikin, R.R., 1950. Winds, Waves and Maritime Structures. Griffin, London, United Kingdom.

Oumeraci, H., Kortenhaus, A., Allsop, W., de Groot, M., Crouch, R., Vrijling, H., Voortman, H., 2001. Proverbs: Probabilistic Design Tools for Vertical Breakwaters. Balkema, Lisse.

Peregrine, D.H., 2003. Water-wave impact on walls. Annu. Rev. Fluid Mech. 35, 23–43.

Peregrine, D.H., Thais, L., 1996. The effect of entrained air in violent wave impacts. J. Fluid Mech. 325, 377–397.

Ramkema, C., 1978. A model law for wave impacts on coastal structures. In: Proc. Coastal Engineering Conference 1978, Hamburg, Germany.

Renzi, E., Wei, Y., Dias, F., 2018. The pressure impulse of wave slamming on an oscillating wave energy converter. J. Fluid Struct. 82, 258–271.

Richert, G., 1968. Experimental investigation of shock pressures against breakwaters. In: Proc. Coastal Engineering Conference 1968, London, United Kingdom.

Takahashi, S., Tanimoto, K., Shimosako, K., 1994. A proposal of impulsive pressure coefficient for design of composite breakwaters. In: Proc. International Conference of Hydro-Technical Engineering for Port and Harbour Construction 1994, Yokosuka, Japan.

Tieleman, O.C., Tsouvalas, A., Hofland, B., Jonkman, S.N., 2019. A three dimensional semi-analytical model for the prediction of gate vibrations. Mar. Struct. 65, 134–153.

Van der Meer, J.W., Allsop, N.W.H., Bruce, T., De Rouck, J., Kortenhaus, A., Pullen, T., Schüttrumpf, H., Troch, P., Zanuttigh, B., 2018. Eurotop, Manual on Wave Overtopping of Sea Defences and Related Structures. An Overtopping Manual Largely Based on European Research, but for Worldwide Application, second ed. www.overtopping-manual.com.

WL, 1977. Wave impacts on the gate in the Eastern Scheldt caisson (In Dutch: Golfklappen op de schuif in de oosterschelde-caisson, Verslag M 1335 deel I). WL Delft Hydraulics (presently Deltares), Delft, The Netherlands.

WL, 1979. A piston model with compressible water (In Dutch: Golfklappen: Een Zuigermodel Met Samendrukbaar Water, Verslag M 1335 Deel II). WL Delft Hydraulics (presently Deltares), Delft, The Netherlands.

WL, 1978. Wave impacts against concrete perforated gates (In Dutch: Golfklappen Tegen Betonnen Roosterschuiven, Verslag M 1381 Deel II). WL Delft Hydraulics (presently Deltares), Delft, The Netherlands.

WL, 1979. A literature review and scale effects in model studies (In Dutch: Golfklappen: een literatuuroverzicht en schaaleffekten in modelonderzoek, Verslag M 1335 deel III). WL Delft Hydraulics (presently Deltares), Delft, The Netherlands.

Wood, D.J., Peregrine, D.H., 1996. Wave impact beneath a horizontal surface. In: Proc. Coastal Engineering Conference 1996, Orland, United States.

Wood, D.J., Peregrine, D.H., Bruce, T., 2000. Study of wave impact against a wall with pressure-impulse theory. i: trapped air. J. Waterw. Port, Coast. Ocean Eng. 126 (4), 182–190.

Zelt, J., Skjelbreia, J., 1992. Estimating incident and reflected wave fields using an arbitrary number of wave gauges. In: Proc. Coastal Engineering Conference 1992, Venice, Italy.